ADVANCED FUNCTIONAL MATERIALS
www.afm-journal.de

Functionalized Graphene as an Electron-Cascade Acceptor for Air-Processed Organic Ternary Solar Cells

Francesco Bonaccorso, Nikolaos Balis, Minas M. Stylianakis, Marika Savarese, Carlo Adamo, Mauro Gemmi, Vittorio Pellegrini, Emmanuel Stratakis, and Emmanuel Kymakis**

Functionalized graphene nanoflakes (GNFs) are used as an electron-cascade acceptor material in air-processed organic ternary bulk heterojunction solar cells. The functionalization is realized via the attachment of the ethylenedinitrobenzoyl (EDNB) molecule to the GNFs. Simulation and experimental results show that such nanoscale modification greatly influences the density of states near the Fermi level. Consequently, the GNF-EDNB blend presents favorable highest occupied molecular orbital and lowest unoccupied molecular orbital energy levels to function as a bridge structure between the poly[*N*-9′-heptadecanyl-2,7-carbazole-alt-5,5-(4′,7′-di-2-thienyl-2′,1′,3′-benzothiadiazole)] (PCDTBT) and the [6,6]-phenyl-C71-butyric-acid-methyl-ester ($PC_{71}BM$). The improved exciton dissociation and charge transport are associated with the better energy level alignment of the ternary blend and the high electrical conductivity of the GNFs, which act as additional electron transport channels within the photoactive layer. The resulting PCDTBT/GNF-EDNB/$PC_{71}BM$ ternary organic solar cells, fabricated entirely under ambient conditions, exhibit an average power conversion efficiency enhancement of ≈18% as compared with the binary blend PCDTBT/$PC_{71}BM$.

1. Introduction

Bulk heterojunction (BHJ) organic solar cells (OSCs) are attracting interest for solar energy conversion due to their potential advantages, with respect to other photovoltaic (PV) technologies,[1] in preparing efficient, flexible, transparent, light-weight, large-area, and low-cost devices.[2–4] To date, power conversion efficiencies (PCE) of BHJ OSCs based on polymer and fullerene derivatives are around 10%[5,6] mainly due to advances on the rational design of low-bandgap polymers, fine control of the photoactive layer's nanomorphology and by interface engineering.[7] However, further improvements in the performance of BHJ solar cells can be foreseen only if many limiting factors, such as insufficient light absorption, nonoptimized morphologies, and low charge carrier mobilities of the active layer materials[8] will be addressed and optimized.

The most successful development of OSCs over the last decade is based on the binary BHJ concept,[9] where a polymer donor and a fullerene acceptor are blended on a nanometer scale.[9] The polymer (i.e., the donor) should exhibit strong and broad absorption band in visible and near infrared regions as long as high hole mobility to transport carriers effectively toward the anode, while the fullerene (i.e., the acceptor) should have higher lowest unoccupied molecular orbital (LUMO) than the polymer, coupled with high electron mobility.[10] In terms of OSC optimization, a simple approach relies on the decrease

Dr. F. Bonaccorso, Dr. V. Pellegrini
Istituto Italiano di Tecnologia
Graphene Labs
I-16163 Genova, Italy
E-mail: francesco.bonaccorso@iit.it
Dr. N. Balis, Dr. M. M. Stylianakis, Dr. E. Stratakis, Prof. E. Kymakis
Technological Educational Institute (TEI) of Crete
Center of Materials Technology and Photonics and Electrical Engineering Department
Estavromenos 1939, Heraklion GR-71 004, Crete, Greece
E-mail: kymakis@staff.teicrete.gr
M. Savarese, C. Adamo
Istituto Italiano di Tecnologia
CompuNet
I-16163 Genova, Italy
Prof. C. Adamo
PSL Research University
Chimie ParisTech-CNRS
Institut de Recherche de Chimie Paris
F-75005 Paris, France
Prof. C. Adamo
Institut Universitaire de France
103 Bd Saint-Michel, F-75005 Paris, France
Dr. M. Gemmi
Center for Nanotechnology Innovation@NEST
Istituto Italiano di Tecnologia
I-56127 Pisa, Italy
Dr. E. Stratakis
Institute of Electronic Structure and Laser (IESL)
Foundation of Research and Technology Hellas (FORTH)
Heraklion, Crete, Greece

DOI: 10.1002/adfm.201501052

of the recombination of the photogenerated electrons and holes through reduction of the energy charge transfer barriers for both electrons and holes within the active layer.[11] An additional challenging and potentially powerful strategy is the addition of a third component into the polymer–fullerene binary blend, leading to the so-called ternary blend solar cell structure.[12] Following this approach, the energy levels of the additive (i.e., the third component) should have the proper offset with respect to the polymer and the fullerene. Contrary to the tandem OSCs with a complex multilayer stack and an additional requirement of a robust intermediate layer,[13] the ternary OSC is actually a single BHJ OSC, where the additive acts as an additional optical absorber, providing complementary absorption,[14,15] or an efficient exciton dissociation center and charge carrier pathway.[16] So far, ternary OSCs have been successfully realized by either mixing fullerenes with two donor polymers[17,18] or mixing poly(3-hexylthiophene-2,5-diyl) (P3HT) with two different fullerene derivatives.[19,20] In the first case, the exploitation of two donor polymers with different ranges of absorption and one fullerene acceptor results in an improvement in the photocurrent via increased light absorption.[21] While in the second case, the use of another fullerene derivative, such as indene-C_{60} bisadduct, which plays a bridging role between the polymer and the fullerene, increases the PCE by providing more routes for charge transfer at the donor/acceptor (D/A) interface.[20] In this context, an alternative strategy is the incorporation of solution processable nanostructures, such as functionalized carbon nanotubes (CNTs) with high charge carrier mobility, providing additional percolation pathway for efficient exciton dissociation and charge transport.[22–24] However, their application is problematic due to lack of control of CNT bandgaps linked to the limited chirality controlled growth[25–27] and the difficulty in the post-processing sorting of metallic/semiconducting CNTs.[28–32] The excitons in the polymer phase ideally diffuse to the polymer–nanotube interface, and the electrons are transferred to the CNT, leaving the hole behind.[33] However, recombination takes place via hole blocking within the tube due to the lack of a bandgap.[34,35] In this context, a solution processable material, which combines the high carrier mobility of CNTs (>10^5 cm^2 V^{-1} s^{-1} at room temperature, RT),[36] and with the energy levels placed between the polymer and the fullerene ones, is highly desirable.

Graphene flakes[37] and graphene derivatives[38] (e.g., graphene oxide —GO— and reduced graphene oxide —RGO—) showcase several key properties[39] that can address emerging energy needs in a variety of PV devices.[40–42] In particular, graphene[37] as well as GO[43] and RGO[38,44] flakes have been exploited as additives in BHJ OSCs to increase their PCE. Jun et al. exploited *n*-doped RGO (*n*-RGO) as the additive material in poly(3-hexylthiophene):methanofullerene (P3HT:PCBM) and reported a PCE enhancement due to higher charge carriers mobility with respect to the P3HT:PCBM device.[38] However, the RGO and *n*-RGO used have a work function of 4.4 and 4.8 eV respectively, as calculated by ultraviolet photoelectron spectroscopy,[38] establishing an energetically favorable offset between the P3HT or the PCBM and the *n*-RGO only for electron transport. In contrast, the absence of a bandgap makes the flakes to act as recombination centers in the BHJ, since an energy band offset is present only for electron transport. Therefore, *n*-RGO flakes cannot be considered as an energy-cascade material for ternary OSCs.[38] Indeed Jun et al., exploiting *n*-RGO in ternary OSCs, reported a modest increase in the photocurrent of the ternary device with respect to the binary blend-based one.[38] Robaeys et al. used solution-processed graphene flakes, obtained from the exfoliation of pristine graphite, as the additive in P3HT:PCBM OSC.[37] It was shown that the graphene addition determines the formation of a continuous active film with interpenetrating structure by improving the crystallinity of the P3HT.[37] Nevertheless, similar to the *n*-RGO case,[38] solution-processed graphene flakes cannot be considered as an energy-cascade component in a ternary BHJ solar cell due to lack of a bandgap, and thus energy level matching.[37] Contrary, solution-processed graphene flakes can be considered as an additive to improve the crystallization and morphology of P3HT as well as the charge transport properties.[37] The improvement of charge transport properties, with respect to the standard P3HT:PCBM OSC, is ascribed to a better balancing between electron and hole mobilities due to graphene flakes addition.[37]

Here, we exploit graphene nanoflakes (GNFs) with controlled lateral size and functionalized with 3,5-dinitrobenzoyl (EDNB) as a ternary compound acting as an efficient electron-cascade acceptor material in combination with poly[*N*-9′-heptadecanyl-2,7-carbazole-alt-5,5-(4′,7′-di-2-thienyl-2′,1′,3′-benzothiadiazole)] PCDTBT and [6,6]-phenyl-C71-butyric-acid-methyl-ester $PC_{71}BM$ (PCDTBT/$PC_{71}BM$) OSC. The idea originates from model calculations based on a density functional theory (DFT) approach that demonstrate the possibility to tune the GNF electronic properties in order to open a bandgap, achieving a fine tuning of both the highest occupied molecular orbital (HOMO) and LUMO energy values of the GNFs. The functionalization process permits us to tune the HOMO and LUMO levels of the GNFs between the HOMOs and the LUMOs of the host polymer and fullerene components. The resulting OSC shows an increase of 18% in PCE, achieving a value of 6.41%, with respect to the binary OSC (PCE = 5.44%). These results open a new pathway toward the technological exploitation of OSCs.

2. Results and Discussion

2.1. Theoretical Background

The GNF-EDNB model systems considered in our simulations are shown in **Figure 1**. These systems result from a study concerning different structural models, as detailed in the Supporting Information. In PV applications, the orbital energies can be considered as one of the most indicative parameters, since a correct energy matching between the orbitals of the donor and the acceptor assures an efficient electron transport.

The electronic properties of the "model GNFs" (M-GNFs) are strongly affected by several factors, including the anchor site of EDNB (edge vs basal), the number of epoxidic groups and the presence of a solvent (here *N*,*N*-dimethylformamide, DMF, see the Experimental Section). It should be pointed out that epoxidic functionalization is a prerequisite necessary to introduce larger substituents,[45] but we anticipate that a subtle control of the number and positions of epoxidic oxygens (EPO) is not

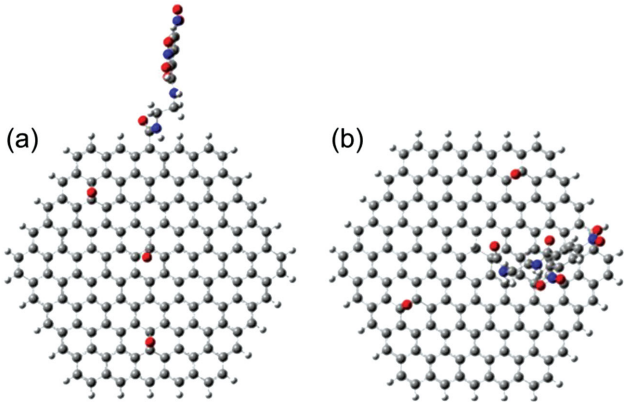

Figure 1. Structure of the two M-GNFs considered, with the EDNB ligand in a) the periphery and b) the center of the molecular structure. Red and blue dots are oxygen and nitrogen atoms, respectively.

possible at the experimental level. Therefore, starting from the selected M-GNFs, formed by 61 fused benzenic cycles, a lateral chain of EDNB was added on the bare GNF, as well as, up to four EPOs randomly placed on the GNF. **Figure 2** reports the energies of the HOMO and LUMO, respectively, with respect to the GNF functionalization, as well as the corresponding gap. The HOMO and LUMO energies of the M-GNFs are computed at –5.1 and –2.8 eV, leading to a gap of 2.3 eV.[46] The functionalization with the EDNB molecule enhances the HOMO–LUMO gap of the M-GNFs by 0.41 eV, through an indirect stabilization of the HOMO (–0.29 eV) and destabilization of the LUMO (+0.09 eV). This effect is in line with previous experimental and theoretical results on graphene functionalization.[47,48]

Epoxidic oxygens have, instead, an opposite effect leading to a reduction of the HOMO–LUMO gap. Indeed, a decrease of about 0.5 eV of the gap is observed upon insertion of three or four oxygen atoms into the molecular structure (see Figure 2). The combination of the two opposite effects leads to a gap for the GNF functionalized with one EDNB chain and three epoxydic oxygens, due to the destabilization of the HOMO and stabilization of the LUMO with respect to GNF, as it appears from the data reported in Figure 2. However, the obtained value is close to that of the pristine GNF (2.2 vs 2.3 eV, respectively). The presence of the solvent induces an energetic stabilization that is similar for both HOMO and LUMO (about –0.15 eV), which are computed at –5.5 and –3.3 eV, respectively. These two values have to be considered as our best estimate of the two orbital energies. Thus, our computations show that GNF functionalization leads to an energy stabilization of both HOMO and LUMO orbitals, thus predicting a better energy levels match with the frontier orbitals of the two other components of the cells, namely PCDTBT and $PC_{71}BM$. Indeed the experimental HOMO energy of PCDTBT is around –5.3 eV,[49] slightly higher in energy than the computed value of GNF-EDNB (–5.5 eV). The experimental LUMO is around –3.3 eV,[49] matching our theoretical value for the functionalized GNF (which could be overestimated by the DFT calculation). On the other hand, the HOMO/LUMO levels of $PC_{71}BM$ (estimated at –5.8 and –4.0 eV at experimental level[49] are both lower in energy than the corresponding orbitals of GNF-EDNB. Thus, our calculations predict a favorable energy alignment for the three components of the cells and well illustrate how the on-demand tuning, by chemical functionalization, of the GNF electronic properties is a promising route for the optimization of PV devices.

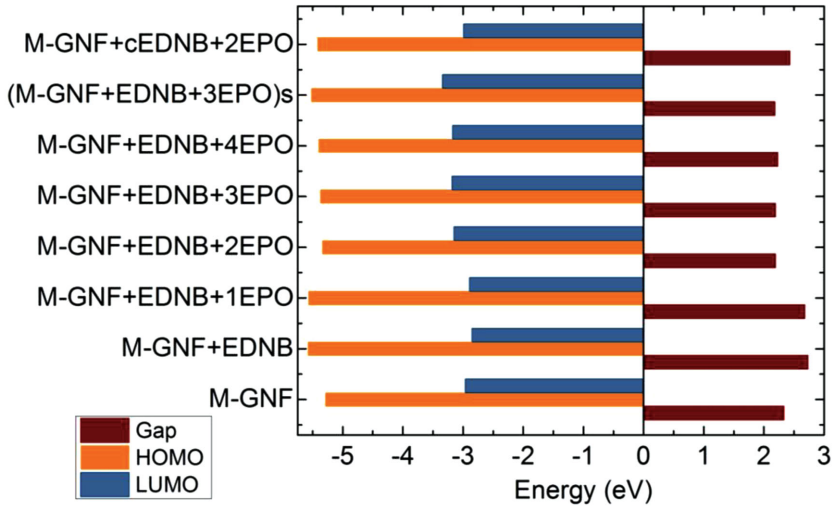

Figure 2. Frontier orbital energies and HOMO/LUMO gap for the considered M-GNFs. cEDNB refers to system with central EDNB and s stands for solvent.

2.2. Experimental Results

Graphene nanoflakes in the form of an ink were prepared dispersing graphite flakes in *N*-methyl-2-pyrrolidone (NMP). The choice of graphite exfoliation in NMP is set by the need of a subsequent functionalization of the graphene flakes, which, for example, could be affected by the presence of surfactant molecules in aqueous solutions.[50,51] The initial dispersion was then ultrasonicated for 6 h. During the ultrasonication process, the strong hydrodynamic shear force, created by the propagation of cavitons,[52] i.e., the creation and subsequent collapse of bubbles or voids in liquids due to pressure fluctuations,[52] induces exfoliation of the graphitic flakes.[53] However, the exfoliation process produces a heterogeneous dispersion of thin/thick and small/large graphitic flakes.[54] After exfoliation, the solvent–graphene interaction needs to balance the interflakes attractive forces that cause reaggregation.[53,54] The obtained dispersion was subsequently ultracentrifuged exploiting the sedimentation-based separation (SBS) to sort small lateral size (≈100 nm) GNFs.[50,55]

We used optical absorption spectroscopy (OAS) in order to evaluate the concentration of graphitic material in the ink. **Figure 3**a plots the OAS of the ink prepared via SBS. The UV absorption peak at ≈266 nm is attributed to inter-band electronic transitions from the unoccupied π^* states at the M point of the Brillouin zone.[56,57] The asymmetry of the UV peak, with a high-wavelength tail, is attributed to excitonic effects.[57,58] Using the

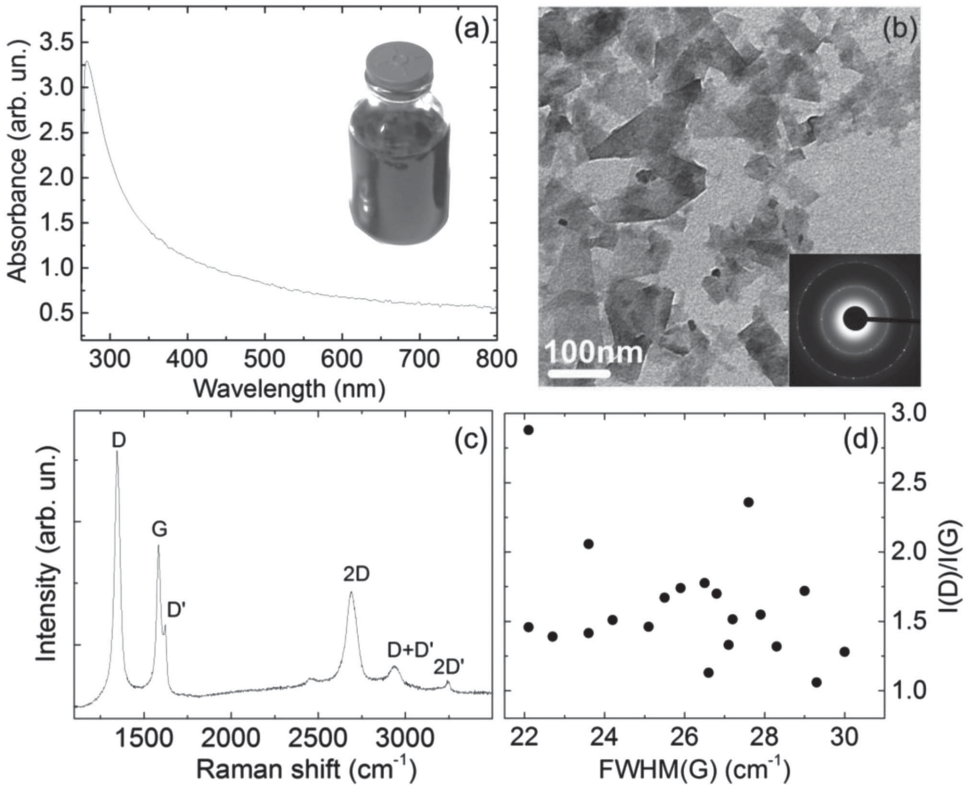

Figure 3. Characterization of GNFs ink. a) RT absorption spectrum of the SBS graphene ink. Inset: Photograph of graphene ink. b) Bright-field TEM image of graphene flakes at high magnification. Inset: Electron diffraction pattern collected on an area of 2 μm in diameter. The 10–10 and 11–20 polycrystalline diffraction rings of graphene are clearly visible. The rings are formed by strong spots corresponding to the larger flakes and a background of weaker unresolved spots associated with smaller flakes. c) Raman spectrum measured at 532 nm laser excitation wavelength for a representative flake obtained via sedimentation-based separation. d) $I(D)/I(G)$ as a function of FWHM(G) measured on flakes deposited on Si/SiO_2.

experimentally derived absorption coefficient of 1390 L g^{-1} m^{-1} at 660 nm[53,81] we estimate a concentration of graphitic material in the ink of ≈54 mg L^{-1}.

Figure 3b plots a low-resolution transmission electron microscopy (TEM) bright field image revealing a large quantity of graphene flakes deposited on the TEM grid. The flakes have lateral size dimensions mostly in the range ≈30–150 nm. Electron diffraction pattern, shown in the inset of Figure 3b, collected on flake aggregates shows polycrystalline rings demonstrating that the flakes are crystalline. All the rings can be indexed as $h, k, -h-k, 0$ reflections of an hexagonal lattice with $a = 0.244(1)$ nm, in agreement with the graphene structure.[59]

Figure 3c plots a typical Raman spectrum of the flakes deposited on Si/SiO_2. Raman spectroscopy is a fast and non-destructive technique to identify number of layers, doping, defects, disorder, chemical modifications, and edges of graphitic flakes.[60,61] In a typical Raman spectrum of graphene, the G peak corresponds to the E_{2g} phonon at the Brillouin zone center.[61] The D peak is due to the breathing modes of sp^2 rings and requires a defect for its activation by double resonance.[60–63] The 2D peak is the second order of the D peak.[62] This is a single peak in monolayer graphene, whereas it splits in multilayer graphene, reflecting the evolution of the band structure.[62] The 2D peak is always seen, even when no D peak is present, since no defects are required for the activation of two phonons with the same momentum, one backscattered from the other.[62] Double resonance can also happen as intravalley process, i.e., connecting two points belonging to the same cone around K or K'.[62] This process gives rise to the D' peak. The 2D' is the second order of the D'.[61]

Statistical analysis, carried out on more than 30 measurements, of the micro-Raman spectra (see Figure S6 in the Supporting Information for more details) shows that the position of the 2D peak (Pos(2D)) is peaked at ≈2691 cm^{-1}, while the full-width at half-maximum (FWHM) (2D) ranges from 60 to 95 cm^{-1} with a peak at ≈72 cm^{-1}, while $I(2D)/I(G)$ varies from 0.65 to 1.1. This is consistent with the samples being a combination of single layer (SLG) and few-layer graphene (FLG) flakes. The Raman spectrum shows (Figure 3c) significant D and D' peaks intensity, with an average intensity ratio $I(D)/I(G)$ ≈1.4, see Figure S6 (Supporting Information). This is attributed to the edges of our submicrometer flakes[64] rather than to the presence of a large amount of structural defects within the flakes. This observation is supported by the lack of a clear correlation between $I(D)/I(G)$ and FWHM(G) (see Figure 3d), which is an indication that the major contribution to the D peak comes from the sample edges.[50]

The schematic illustration of the graphene ink functionalization process to yield GNF-EDNB is depicted in **Figure 4**a. Both the initial and functionalized graphene were characterized by Fourier transform infrared (FT-IR) spectroscopy. Figure 4b shows the FT-IR spectra of the materials

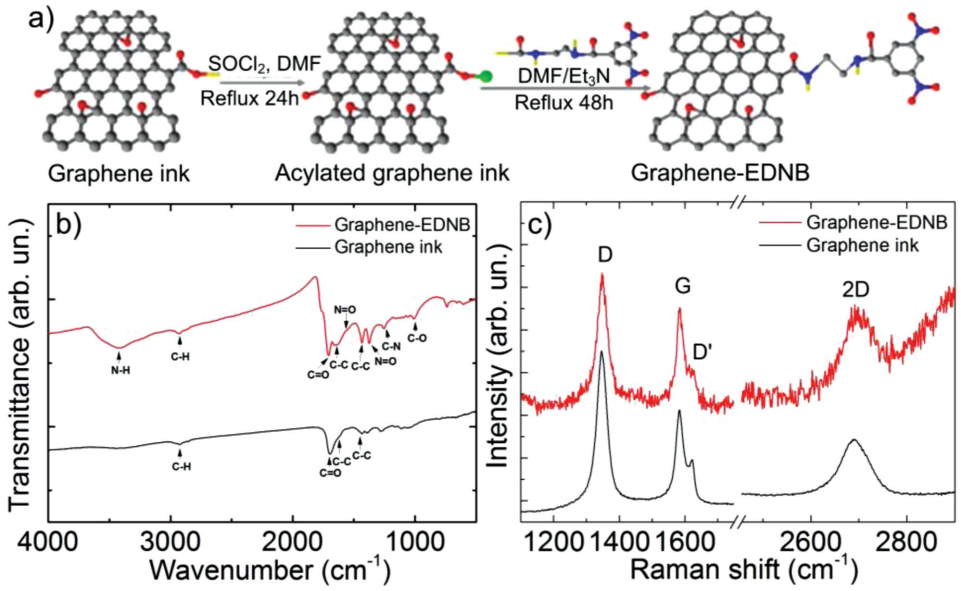

Figure 4. a) Schematic illustration of the graphene functionalization process. b) FT-IR spectra of graphene ink (black curve) and graphene-EDNB (red curve). The main peaks are indicated in the graphs. c) Raman spectra of graphene ink (black curve) and graphene-EDNB (red curve).

confirming the successful linkage of nitro moieties to the graphene lattice via amide linkage. More specifically, the black line in Figure 4b, corresponding to graphene ink, depicts a broad aliphatic peak (C—H) at 2924 cm^{-1},[65] the C=O peak (i.e., carbonyl moieties) at 1697 cm^{-1} and the peak at 1625 cm^{-1} associated with C—C graphitic domains.[66] On the other hand, GNF-EDNB spectrum (red line) exhibits a broad peak at 3420 cm^{-1} (N—H stretching bond)[67] and a broad and weak aliphatic peak at 2930 cm^{-1} (C—H stretching).[65] The peak at 1710 cm^{-1}[68] corresponds to the C=O stretching, while the stretching bands of C=O and C—N, attributed to the amide bond, appear at 1653 cm^{-1}[68,69] and 1254 cm^{-1},[68] respectively. The band in the 1000–1200 cm^{-1} range contains weak peaks of carbonyl (C—O) groups.[70] The peak corresponding to C—C stretching of the aromatic EDNB ring is also displayed at 1430 cm^{-1}. Finally, the peaks at 1555 and 1375 cm^{-1} are attributed to the characteristic of the nitro groups (N—O)[71] attached to graphene lattice of GNF-EDNB. Thus, the FT-IR spectrum of the GNF-EDNB sample indicates the successful linkage between the acylated GNF ink and dinitrobenzoyl chloride via ethylenediamine.

The Raman spectrum of the GNF-EDNB ink (red curve in Figure 4c) shows Pos(G) and Pos(2D) upshifted, ≈3 and ≈8 cm^{-1}, respectively, with respect to their counterparts in the GNF ink (black curve in Figure 4c), which could be ascribed to doping[62] of the GNF due to EDNB linkage. However, the 2D peak still shows a lineshape distinctly different from that of graphite.[72] This implies that the flakes are still either SLG or FLG and that the functionalization process does not induced aggregation of the flakes. Moreover, from Raman analysis, and in particular from the $I(D)/I(G)$ ratio, we can evaluate that there are not structural defects on the GNFs following the EDNB functionalization process.

In order to assess the changes in the electronic bandgap resulting from graphene functionalization, cyclic voltammetry (CV) measurements (see Figure S7 in the Supporting Information) were carried out on GNF-EDNB derivatives produced at different functionalization times (GNF-EDNB12, GNF-EDNB24, GNF-EDNB48, and GNF-EDNB60, prepared using functionalization times of 12, 24, 48, and 60 h, respectively). The HOMO and LUMO levels were gathered from their respective ionization potentials and electron affinities, estimated from the first oxidation and reduction onset potentials (see Figure S7 in the Supporting Information) according to the following formulas:[73]

$$E_{HOMO} = -(E_{[onset,ox\,vs\,Fc+/Fc]} + 5.1)(eV) \quad (1)$$

$$E_{LUMO} = -(E_{[onset,red\,vs\,Fc+/Fc]} + 5.1)(eV) \quad (2)$$

Table 1 summarizes the HOMO–LUMO levels of the four different GNF-EDNB derivatives obtained from Equations (1) and (2). It is observed that the total functionalization time of solid acylated graphene ink (GNF-Cl) to GNF-EDNB plays crucial role toward tuning of the GNF bandgap. From the HOMO–LUMO values reported in Table 1, the reaction time of 60 h appears as the most appropriate in order to get a full reaction of the GNF-Cl groups with the amino groups of EDNB, forming stable amide bonds (GNF-EDNB) with a wide bandgap. Upon

Table 1. HOMO and LUMO values for different GNF-EDNB samples as measured by CV.

Sample	HOMO [eV]	LUMO [eV]
GNF-EDNB12	–4.9	–4.4
GNF-EDNB24	–5.2	–4.1
GNF-EDNB48	–5.7	–3.9
GNF-EDNB60	–5.7	–3.9
GNF-EDNB120	–5.7	–3.9

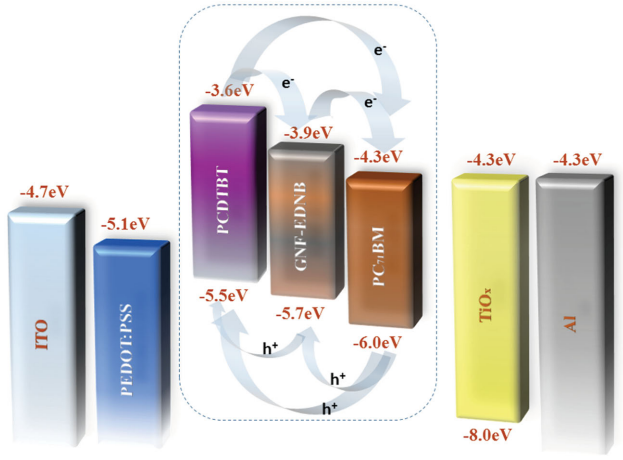

Figure 5. Energy level diagram of a ternary OSC clearly illustrating the cascade charge transport, where the PCDTBT:$PC_{71}BM$ is employed as the host system and the GNF-EDNB60 as an electron-cascade acceptor. The values of the HOMO–LUMO energy levels correspond to GNF-EDNB60 (see Table 1).

further increasing of the reaction time (>60 h), no additional variation of the electronic bandgap value was observed.

Figure 5 displays the energy diagram of the materials used for fabricating the OSC as well as the charge generation and transfer procedures between the third components of the blend. The HOMO and LUMO energy levels of PCDTBT and $PC_{71}BM$ were taken from the literature.[49] The observed bandgap opening in the GNF-EDNB60 blend is in line with our calculations on model systems reported in Section 2.1 and, as already mentioned, can be associated with the chemical modification of the graphene flakes by organic molecules. This effect is additionally supported by recent DFT calculations.[50]

In a binary OSC (i.e., PCDTBT:$PC_{71}BM$) the excitons diffuse at the donor material and dissociation occurs at the PCDTBT:$PC_{71}BM$ interface through electron migration to the LUMO of $PC_{71}BM$, see Figure 5. On the contrary, in the case of our ternary OSC, exciton dissociation can occur at both PCDTBT:$PC_{71}BM$ and PCDTBT:GNF-EDNB interfaces. As can be seen from Table 1, amongst the synthesized GNF-EDNB derivatives, the electronic structure of GNF-EDNB60 is the most suitable to reach our goal, i.e., increase charge carriers mobility. Indeed, the HOMO and LUMO levels of GNF-EDNB60 are properly located at –5.7 eV and 3.9 eV respectively, with respect to the polymer–fullerene blend, and in good agreement with the computed data (–5.5 and –3.3 eV, respectively), reported in Section 2.1. The HOMO and LUMO levels of GNF-EDNB60 are located between the HOMO and the LUMO energy levels of $PC_{71}BM$ and PCDTBT, respectively. Therefore, a favorable energy alignment between the LUMO and HOMO levels enables GNF-ENBD60 to function as an energy-gradient bridge, so that electrons can efficiently be transported to the cathode and holes to the anode through the energetic downhill cascade pathways (arrows in Figure 5). Thus, in our OSC we foreseen three routes (PCDTBT:$PC_{71}BM$, PCDTBT:GNF-EDNB60, and GNF-EDNB60:$PC_{71}BM$) for charge transfer, contrary to the counterpart binary OSC where only one route for charge transfer (PCDTBT:$PC_{71}BM$) is possible.

2.2.1. Charge Transfer Processes

To get a more accurate insight into the influence of GNF-EDNB blend into the charge transfer process in the air assembled OSC, hole-only and electron-only cells were fabricated in order to calculate the hole and electron mobility, respectively. Measurements were based on space charge limited current method.[74] Hole-only cells and electron-only cells were fabricates using the architecture indium tin oxide (ITO)/poly(3,4-ethylenedioxythiophene):poly(styrene sulfonate) (PEDOT:PSS)/PCDTBT:GNF-EDNB60:$PC_{71}BM$/Au for holes and ITO/Al/PCDTBT:GNF-EDNB60:$PC_{71}BM$/Al for electrons, respectively. The evaluation of the charge carrier mobilities was based on the Mott–Gurney equation:[75]

$$J_{SCLC} = 9/8\varepsilon_r \varepsilon_0 \mu (V - V_{bi})/d^3 \quad (3)$$

where ε_r is the relative dielectric constant, ε_0 is the permittivity of free space, μ is the charge carrier mobility, V is the applied voltage, V_{bi} is the built-in potential, and d is the thickness of the active layer.

Figure 6a,b illustrates the J–V characteristics under dark conditions for hole-only and electron-only cells, respectively. Control device (black line) refers to a OSC with the binary blend PCDTBT:$PC_{71}BM$, while "GNF-EDNB" (red line) refers to a cell

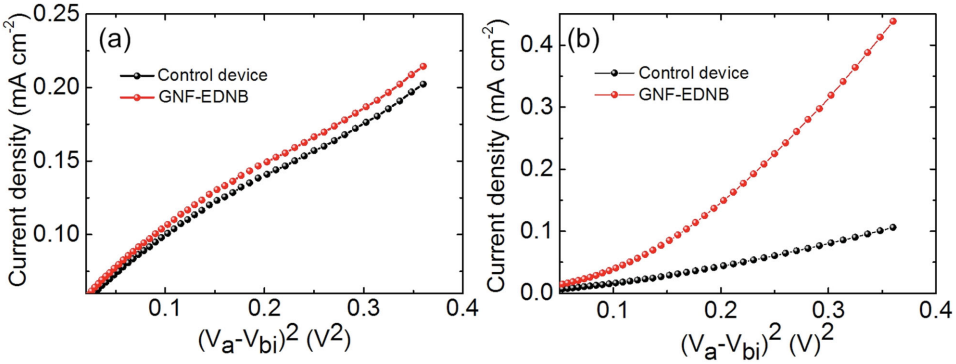

Figure 6. Representative J–V characteristics under dark conditions for a) hole-only and b) electron-only cells with (red curve) and without (black curve) GNF-EDNB60.

based on the ternary blend PCDTBT:GNF-EDNB60:$PC_{71}BM$, containing 0.05% by volume of GNF-EDNB60. The *J–V* characteristic shows that while hole mobility was only slightly increased from 1.7×10^{-5} cm^2 V^{-1} s^{-1} (for the PCDTBT:$PC_{71}BM$-based OSC) to 1.8×10^{-5} cm^2 V^{-1} s^{-1} for the ternary blend PCDTBT:GNF-EDNB60:$PC_{71}BM$-based OSC (see Figure 6a), the electron mobility has instead shown a significant increase, passing from 2.3×10^{-5} cm^2 V^{-1} s^{-1} for the control cell to 5.9×10^{-5} cm^2 V^{-1} s^{-1} for the PCDTBT:GNF-EDNB60:$PC_{71}BM$-based cell. This improvement in electron mobility originates from the presence of additional dissociation interfaces (PCDTBT:GNF-EDNB60), and the existence of additional high conductive pathways in the active layer, facilitated by the optimization of the energy levels matching and the high electrical conductivity of GNFs.[55] Although the significant difference in the improvement of the hole and electron mobilities is presently unclear, the observed carrier transport enhancement is associated to the cascade energy levels in the ternary OSC.

To further investigate the cells' performance, we also measured the maximum exciton generation rate (G_{max}) and exciton dissociation probabilities $P(E,T)$, which is related to the electric field (E) and temperature (T), of our OSCs, see Figure S8 (Supporting Information). The values of G_{max} for the binary and GNF-EDNB-based OSCs are 8.11×10^{27} and 9.04×10^{27} s^{-1} cm^{-3}, respectively. The slight increase in G_{max} in the GNF-EDNB60-based ternary OSC could be ascribed to a slight increase in light absorption (Figure S9, Supporting Information) and therefore due to the incorporation of GNF-EDNB60 in the active layer. Moreover, the $P(E,T)$ also increased from 91% for the control OSC to 93% for the GNF-EDNB60-based ternary OSC, indicating a slight decrease in the recombination rate, which consequently improves the OSC fill factor (FF) (**Table 2**).

2.2.2. Solar Cells

Figure 7a shows a schematic representation of a typical sandwich structure of ITO/PEDOT:PSS/PCDTBT:$PC_{71}BM$:GNF-EDNB60/TiO_x/Al ternary BHJ OSCs. The inner structure of the PCDTBT:$PC_{71}BM$:GNF-EDNB blend is also shown.

Figure 7b displays the illuminated *J–V* curves measured under one-sun irradiation. We fabricated and measured solar cells without any GNF-EDNB (control OSC based on a binary PCDTBT:$PC_{71}BM$ blend), with 0.05% GNF-EDNB60, 0.10% EDNB60, and 0.15% EDNB60 by volume, respectively. The control OSC exhibits a $V_{OC} \approx 884$ mV, a short circuit current density (J_{sc}) ≈ 11.40 mA cm^{-2} and an FF ≈ 54.2% resulting in a total PCE up to ≈5.59%. The presence of GNF-EDNB blend has beneficial influence on the PV performances of the final cell. At lower concentrations of GNF-EDNB (0.05% and 0.10%) in the ternary blend, the solar cells have shown a better PCE performance due to enhancement of all the main figures of merit (FoM) of the cell, i.e., V_{oc}, J_{sc}, and FF, with respect to the control OSC, see Table 1. In particular, the solar cell with 0.05% GNF-EDNB60, exhibits the highest J_{sc} value of 12.56 mA cm^{-2} with V_{oc} = 896 mV and an FF = 57.1%. These values result to a 6.59% PCE for the champion solar cell. By increasing the GNF-EDNB60 concentration (0.10%), the V_{oc} and FF remain stable, while the J_{sc} presents a remarking decrease at 11.95 mA cm^{-2}, with respect to the 0.05% GNF-EDNB60-based OSC, resulting in a PCE = 6.27%.

Further increase of the GNF-EDNB60 concentration (0.15%) leads to a deterioration of all the FoM of the OSCs. Table 2 summarizes the average values (taken from ten identical devices, consisting of six cells each) of the FoM, together with the standard deviations, of OSCs based on PCDTBT:$PC_{71}BM$ with different GNF-EDNB60 content. The numbers reported in parentheses in Table 2 represent the values obtained for the champion OSCs.

Our results demonstrate that high conductive,[55] small lateral size GNFs[55] functionalized with EDNB moieties, offer new percolation pathways to charge carriers, resulting in an increase, with respect to the control cell, of the J_{sc}. Beyond a threshold concentration, which we estimated around 0.10%, the addition of GNF-EDNB60 blend has a negative impact on the PV performances, mainly due to a reduction of J_{sc}, as reported in both Figure 7b and Table 2. The worsening of the PV performances can be explained by the fact that an increase of the GNF-EDNB60 concentration over 0.10%, further increases the electron mobility of the OSCs, resulting in a large imbalance of hole and electron mobilities and hence a decrease in PCE.

Moreover, we have evaluated the series resistance of the binary and the ternary OSCs, estimated to be ≈13.4 and ≈11.9 Ω cm^{-2}, respectively (obtained by the inverse slop of *J–V* curves at the far forward characteristics where the curve becomes linear). The comparison of the series resistance values clearly indicate that GNFs, incorporated into the polymer–fullerene blend, contribute to the charge carrier transport, offering additional pathways for electron transport. Figure 7c shows the external quantum efficiency (EQE) spectra of the binary and ternary OSCs. It can be seen that the EQE enhancement is mainly due to J_{sc} increase. However, the EQE enhancement in the 350–420 nm region follows the absorption enhancement in this specific region (Figure S9, Supporting Information), indicating that the GNF-EDNB60 has also a slight effect in the absorption enhancement, as was quantified in the observed exciton generation rate (Figure S8, Supporting Information). The accuracy of the PV measurements were checked, by calculating the J_{sc} values of the OSCs from the integration of the EQE spectra and were find to be similar to the ones obtained from the *J–V* curves (error is 2.87%).

It should be also noted that any concentration of GNF-EDNB60 higher than 0.15 wt% results to short circuit, probably due to the occurrence of local shunts. This undesired effect could be linked with the concentration of GNFs in the blend that becomes enough to allow a direct bridging with the

Table 2. Average FoM and standard deviations of OSCs based on PCDTBT:$PC_{71}BM$ with different GNF-EDNB60 content. The numbers in parentheses represent the values obtained for the champion OSC.

GNF-EDNB60 ν [%]	J_{sc} [mA cm^{-2}]	V_{oc} [mV]	FF [%]	PCE [%]
0.00	11.40 ± 0.18	884 ± 5	54.2 ± 0.4	5.44 ± 0.15 (5.59)
0.05	12.56 ± 0.35	896 ± 6	57.1 ± 0.5	6.41 ± 0.18 (6.59)
0.10	11.95 ± 0.24	896 ± 6	57.0 ± 0.5	6.10 ± 0.17 (6.27)
0.15	11.17 ± 0.18	889 ± 5	54.4 ± 0.4	5.36 ± 0.15 (5.51)

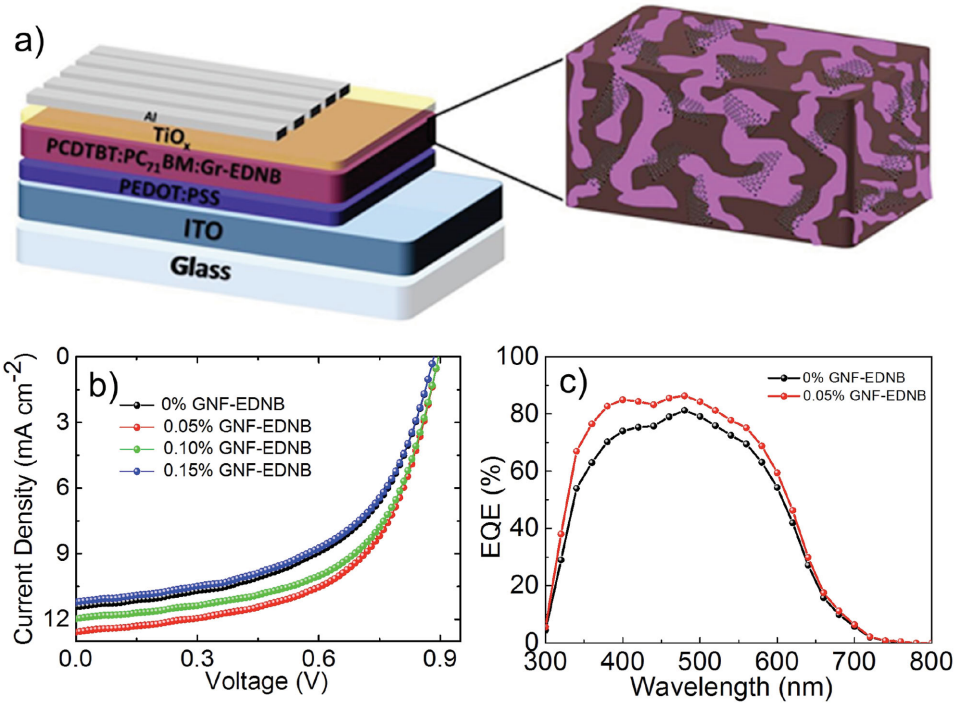

Figure 7. a) Schematic illustration of the ITO/PEDOT:PSS/PCDTBT:$PC_{71}BM$:GNF-EDNB60/TiOx/Al BHJ solar cell, with a close-up on the PCDTBT:$PC_{71}BM$:Gr-EDNB60 ternary blend structure. b) *J–V* characteristics under 1 sun illumination for OSCs with different concentrations of GNF-EDNB60. c) EQE spectra of binary and ternary OSCs.

ITO electrode. Moreover, the favorable energy alignment of the GNF-EDNB60 leads to a slight increase of the V_{oc}, if compared with the binary OSC, since the LUMO of GNF-EDNB60 (–3.9 eV) is slightly shifted above the respective LUMO of the fullerene (4.3 eV) (Figure 5). Finally, the increase of the FF of the GNF-EDNB60-based ternary cell with respect to the standard binary cell (PCDTBT:$PC_{71}BM$ OSCs) could be a direct consequence of the higher electron mobility and higher exciton dissociation.

3. Conclusions

In conclusion, GNF-EDNB was synthesized using graphene produced by liquid phase exfoliation of pristine graphite as the starting material. GNF-EDNB60 was utilized in combination with PCDTBT and PCBM, as an electron-cascade acceptor material in order to engineer ternary OSCs. Due to the on-demand tuning of the energy levels, GNF-EDNB60 plays a crucial role as a highly conductive bridge between polymer chains and fullerene molecules. Its presence offers two interfaces for exciton dissociation as well as multiple routes for charge transfer at the donor/acceptor interfaces. Compared with the binary PCDTBT:$PC_{71}BM$ OSCs, the ternary OSCs with 0.05% GNF-EDNB exhibited higher values of V_{oc}, FF, and J_{sc}, resulting in 18% PCE enhancement. Our best OSC has shown a 6.59% PCE, which is a remarkable high value for completely air-processed OSCs. Our results demonstrate that the exploitation of on-demand functionalized graphene derivatives as an electron-cascade acceptor material is a promising way toward the performance optimization of OSCs based on low-bandgap polymer donors and fullerene acceptors.

4. Experimental Section

Modeling: All the computations were carried out at a DFT level, using the M06-2X functional.[76] This approach is known to provide accurate electronic properties for a large variety of chemical systems.[76] All the M-GNFs were fully optimized using the 6-31+G(d,p) basis set and harmonic frequencies have been computed at the same level of theory in order to assess the nature of the localized structure as energy minima. Solvent effects were included by the means of the polarizable continuum model in the linear response formalism.[77] Finally, in order to allow for a direct comparison with previous results on graphene-like systems,[78] some calculations have been carried out using the Heyd-Scuseria-Ernzerhof (HSE) functional (see the Supporting Information for an in-depth discussion on this topic).[79] All computations were performed using the Gaussian 09 suite of programs.[80]

Experiments: The experimental study was carried out as follows.

Graphene Ink Preparation: The graphene ink used in this work was prepared dispersing 200 mg of graphite flakes (Sigma Aldrich Ltd.) in 20 mL of NMP (Sigma Aldrich Ltd.). The obtained dispersion was subsequently ultracentrifuged using an SW-41 swinging bucket rotor in a Beckman-Coulter Optima XPN ultracentrifuge at 25 000 rpm (≈77 000 g) for 30 min. After ultracentrifugation, the supernatant was extracted by pipetting.

Characterization of Graphene Inks: The measurements were carried out as follows.

Optical Absorption Spectroscopy: Absorption measurements were carried out with a Jasco V-550 UV–vis. The concentration of the ink was determined exploiting the experimentally derived absorption coefficient of 1390 L g^{-1} m^{-1} at 660 nm[53,81] (see S. I.).

Transmission Electron Microscopy: The as-prepared ink was drop casted at room temperature onto carbon coated copper TEM grids (300 mesh) and rinsed with deionized water. TEM images were taken with a Zeiss Libra 120 transmission electron microscope, operated at 120 kV and equipped with an in-column omega filter. All the images and the diffraction patterns were energy filtered with a 15 eV slit on the zero loss peak.

FTIR Spectroscopy: KBr powder was finely pulverized in a mortar and then was put into a pellet-forming die. A force of ≈8 tons was applied, forming a transparent pellet. The pellet was inserted into an empty pellet holder and 10 µL of graphene ink were dropped onto. Then the pellet was dried thoroughly by annealing using a hotplate at 80 °C. The final prepared sample containing graphene ink was analyzed by the BRUKER FT-IR spectrometer IFS 66v/F (MIR). Gr-EDNB powder ≈1 and ≈100 mg of KBr were mixed in the mortar. Afterward, a small amount of the finely crushed mixture was put into a pellet-forming die, forming a slightly colored semitransparent pellet. The pellet was then inserted into an empty pellet holder and was analyzed by the BRUKER FT-IR spectrometer.

Raman Spectroscopy: For Raman measurements, the graphene ink was diluted (1:10) with pure NMP and drop casted onto an Si wafer with 300 nm thermally grown SiO_2. Raman measurements were carried out with a Renishaw 1000 at 532 nm and a 100X objective, with an incident power of ≈1 mW. The D, G, and 2D peaks were fitted with Lorentzian functions.

Acylation of Graphene Ink (GNF-Cl): Graphene ink (10 mL) was evaporated by rotary evaporation, under reduced pressure at 70 °C, in order to remove NMP, to recover it as solid. The yielded powder (≈0.5 mg) was dispersed in thionyl chloride ($SOCl_2$) (0.4 mL) and a catalytic amount of DMF (0.1 mL) was added. The excess of $SOCl_2$ was removed by distillation under reduced pressure[33] The obtained Gi—Cl was washed with ultradried tetrahydrofuran three times, in order to take off the excess of $SOCl_2$ and dried at a temperature of 40 °C in a vacuum oven for 2 h. The yielded GNF-Cl was dried for 3 h at 80 °C.

GNF-EDNB Preparation: G-Cl (1.6 mg) was dispersed in DMF (8 mL) by bath ultrasonication (5 min) at room temperature to give a homogenous dispersion.[82] The initial dispersion was separated into four parts of the same volume. EDNB (0.6 mg) and drops of triethylamine (Et_3N) (≈0.5 mL) were added to each sample and then the mixtures were stirred and refluxed for 12, 24, 48, 60, and 120 h, respectively, under nitrogen (N_2). The aforementioned times were defined as the total functionalization time for each sample, respectively. The five samples obtained were named as GNF-EDNB12, Gr-EDNB24, GNF-EDNB48, GNF-EDNB60, and GNF-EDNB120, respectively. When the mixtures were cooled at room temperature, diethylether (2 mL) was added in order to boost the precipitation of the final product as a brownish solid, which was then collected by filtration. A series of purification steps, for the five different samples, were subsequently performed, each of which comprised ultrasonication (10 min) and centrifugation (5 min at 4200 rpm) to yield the final GNF-EDNB. Finally, the precipitant received was dispersed into a mixture of solvents. In particular 1 mg of each GNF-EDNB sample was dispersed in 1 mL of chlorobenzene: *o*-dichlorobenzene (*o*-DCB) (1:3 v/v) followed by stirring at 70 °C overnight.

PCDTBT: PC71BM and PCDTBT: PC71BM:GNF-EDNB60 Blends Preparation: The PCDTBT:$PC_{71}BM$ dispersion was prepared according to the following procedure: PCDTBT and $PC_{71}BM$ (1:4 w/w), both purchased from Solaris Chem, were dispersed into DCB and *o*-DCB (1:3 v/v) and stirred overnight at 70 °C. Then, the dispersions were mixed with different amounts of GNF-EDNB60 (0.05%, 0.10%, and 0.15% v/v) to obtain the final blends.

Characterization of the Graphene-EDNB Blend: FT-IR spectra were measured on a BRUKER FT-IR spectrometer IFS 66v/F (MIR). For Raman measurements, the graphene-EDNB blend was drop-casted onto an Si wafer with 300 nm thermally grown SiO_2. Raman measurements were carried out in the same conditions reported for the characterization of the ink. Cyclic voltammetry measurements were carried out with an Autolab potentiostat PGSTAT128N.

OSC Fabrication: ITO glass substrates (8–12 Ω sq^{-1}) were thoroughly cleaned by ultrasonic treatment with soap solution, acetone, and isopropanol for 20 min each. After cleaning, the substrates were covered with a poly(3,4-ethylenedioxythiophene):poly(styrene sulfonate) (PEDOT:PSS) layer by spin coating for 60 s at 6000 rpm, obtaining a 30 nm film. Then, the films were baked for 20 min at 120 °C in order to dry any residual moisture. Successively, a 80 nm layer of the photoactive blend of PCDTBT: $PC_{71}BM$ or PCDTBT: $PC_{71}BM$:GNF-EDNB60 was spin coated on top of the PEDOT:PSS layer at 1000 rpm. The cell was dried at 60 °C for 1 min and subsequently a 10 nm TiO_x layer, synthesized as described elsewhere,[83] was spin coated on top of the photoactive layer. Finally a 90 nm Al top electrode was deposited to complete cell's architecture creating an active area of 0.04 cm^2.

OSC Characterization: Current–voltage (*I–V*) and impedance measurements were performed at room temperature using an Agilent B1500A Semiconductor Device Analyzer. For photovoltaic characterization, the OSCs were illuminated, using an aperture mask, with 100 mW cm^{-2} power intensity of white light by an Oriel solar simulator with an Air Mass AM1.5 filter through the glass/ITO side, which was calibrated using an Si diode. The EQE spectra were recorded with by an Enli Technology EQE measurement system (QE-R), and the light intensity at each wavelength was calibrated with a standard single-crystal Si solar cell. All measurements were performed in air immediately after the cell fabrication.

Supporting Information

Supporting Information is available from the Wiley Online Library or from the author.

Acknowledgements

The research leading to these results was funded by the European Union Seventh Framework Programme under Grant Agreement No. 604391 Graphene Flagship.

Received: March 17, 2015
Published online: May 12, 2015

[1] M. A. Green, K. Emery, Y. Hishikawa, W. Warta, E. D. Dunlop, *Prog. Photovolt. Res. Appl.* **2013**, *21*, 827.
[2] G. Zhao, Y. He, Y. Li, *Adv. Mater.* **2010**, *22*, 4355.
[3] Z. He, C. Zhong, S. Su, M. Xu, H. Wu, Y. Cao, *Nat. Photonics* **2012**, *6*, 591.
[4] D. H. Wang, J. K. Kim, J. H. Seo, I. Park, B. H. Hong, J. H. Park, A. J. Heeger, *Angew. Chem. Int. Ed.* **2013**, *52*, 2874.
[5] B. Kan, Q. Zhang, M. Li, X. Wan, W. Ni, G. Long, Y. Wang, X. Yang, H. Feng, Y. Chen, *J. Am. Chem. Soc.* **2014**, *136*, 15529.
[6] J.-D. Chen, C. Cui, Y.-Q. Li, L. Zhou, Q.-D. Ou, C. Li, Y. Li, J.-X. Tang, *Adv. Mater.* **2015**, *27*, 1035.
[7] J. You, L. Dou, K. Yoshimura, T. Kato, K. Ohya, T. Moriarty, K. Emery, C. Chen, J. Gao, G Li, Y. Yang, *Nat. Commun.* **2013**, *4*, 1446.
[8] L. Y. Lu, Z. Q. Luo, T. Xu, L. P. Yu, *Nano Lett.* **2013**, *13*, 59.
[9] G. Yu, J. Gao, J. C. Hummelen, F. Wudl, A. J. Heeger, *Science* **1995**, *270*, 1789.
[10] C. J. Brabec, N. S. Sariciftci, J. C. Hummelen, *Adv. Funct. Mater.* **2001**, *11*, 15.
[11] L. M. Chen, Z. Xu, Z. Hong, Y. Yang, *J. Mater. Chem.* **2010**, *20*, 2575.
[12] T. Ameri, P. Khoram, J. Min, C. J. Brabec, *Adv. Mater.* **2013**, *25*, 4245.
[13] T. Ameri, N. Li, C. J. Brabec, *Energy Environ. Sci.* **2013**, *6*, 2390.
[14] J. S. Huang, T. Goh, X. Li, M. Y. Sfeir, E. A. Bielinski, S. Tomasulo, M. L. Lee, N. Hazari, A. D. Taylor, *Nat. Photonics* **2013**, *7*, 479.

[15] L. Ye, H. Xia, Y. B. Xiao, J. B. Xu, Q. Miao, *RSC Adv.* **2014**, *4*, 1087.
[16] R. A. Street, D. Davies, P. P. Khlyabich, B. Burkhart, B. C. Thompson, *J. Am. Chem. Soc.* **2013**, *135*, 986.
[17] P. P. Khlyabich, B. Burkhart, B. C. Thompson, *J. Am. Chem. Soc.* **2012**, *134*, 9074.
[18] T. Ameri, T. Heumuller, J. Min, N. Li, G. Matt, U. Scherf, C. J. Brabec, *Energy Environ. Sci.* **2013**, *6*, 1796.
[19] H. Kang, K.-H. Kim, T. E. Kang, C.-H. Cho, S. Park, S. C. Yoon, B. J. Kim, *ACS Appl. Mater. Interfaces* **2013**, *5*, 4401.
[20] P. Cheng, Y. Li, X. Zhan, *Energy Environ. Sci.* **2014**, *7*, 2005.
[21] L. Lu, T. Xu, W. Chen, E. S. Landry, L. Yu, *Nat. Photonics* **2014**, *8*, 716.
[22] C. Li, Y. Chen, Y. Wang, Z. Iqbal, M. Chhowalla, S. Mitra, *J. Mater. Chem.* **2007**, *17*, 2406.
[23] M. M. Stylianakis, E. Kymakis, *Appl. Phys. Lett.* **2012**, *100*, 093301.
[24] L. Lu, T. Xu, W. Chen, J. M. Lee, Z. Luo, I. H. Jung, H. I. Park, S. O. Kim, L. Yu, *Nano Lett.* **2013**, *13*, 2365.
[25] L. Ding, A. Tselev, J. Y. Wang, D. N. Yuan, H. B. Chu, T. P. McNicholas, Y. Li, J. Liu, *Nano Lett.* **2009**, *9*, 800.
[26] W. Song, C. Jeon, Y. S. Kim, Y. T. Kwon, D. S. Jung, S. W. Jang, W. C. Choi, J. S. Park, R. Saito, C.-Y. Park, *ACS Nano* **2010**, *4*, 1012.
[27] J. Liu, C. Wang, X. Tu, B. Liu, L. Chen, M. Zheng, C. Zhou, *Nat. Commun.* **2012**, *3*, 1199.
[28] R. Krupke, F. Hennrich, H. von Lohneysen, M. M. Kappes, *Science* **2003**, *301*, 344.
[29] M. Zheng, A. Jagota, M. S. Strano, A. P. Santos, P. Barone, S. G. Chou, B. A. Diner, M. S. Dresselhaus, R. S. McLean, G. B. Onoa, G. G. Samsonidze, E. D. Semke, M. Usrey, D. J. Walls, *Science* **2003**, *302*, 1545.
[30] M. S. Arnold, A. A. Green, J. F. Hulvat, S. I. Stupp, M. C. Hersam, *Nat. Nanotechnol.* **2006**, *1*, 60.
[31] F. Bonaccorso, T. Hasan, P. H. Tan, C. Sciascia, G. Privitera, G. Di Marco, P. G. Gucciardi, A. C. Ferrari, *J. Phys. Chem. C* **2010**, *114*, 17267.
[32] T. Tanaka, H. H. Jin, Y. Miyata, H. Kataura, *Appl. Phys. Express* **2008**, *1* ,114001.
[33] M. M. Stylianakis, J. A. Mikroyannidis, E. Kymakis, *Sol. Energy Mater. Sol. Cells* **2010**, *94*, 267.
[34] E. Kymakis, E. Koudoumas, I. Franghiadakis, G. A. J. Amaratunga, *J. Phys. D: Appl. Phys.* **2006**, *39*, 1058.
[35] J. L. Delgado, P. A. Bouit, S. Filippone, M. Herranz, N. Martin, *Chem. Commun.* **2010**, *46*, 4853.
[36] T. Dürkop, S. A. Getty, E. Cobas, M. S. Fuhrer, *Nano Lett.* **2004**, *4*, 35.
[37] P. Robaeys, F. Bonaccorso, E. Bourgeois, J. D'Haen, W. Dierckx, W. Dexters, D. Spoltore, J. Drijkoningen, J. Liesenborgs, A. Lombardo, A. C. Ferrari, F. Van Reeth, K. Haenen, J. V. Manca, M. Nesladek, *Appl. Phys. Lett.* **2014**, *105*, 083306.
[38] G. H. Jun, S. H. Jin, B. Lee, B. H. Kim, W.-S. Chae, S. H. Hong, S. Jeon, *Energy Environ. Sci.* **2013**, *6*, 3000.
[39] A. C. Ferrari, F. Bonaccorso, V. Falko, K. S. Novoselov, S. Roche, P. Bøggild, S. Borini, F. Koppens, V. Palermo, N. Pugno, J. A. Garrido, R. Sordan, A. Bianco, L. Ballerini, M. Prato, E. Lidorikis, J. Kivioja, C. Marinelli, T. Ryhänen, A. Morpurgo, J. N. Coleman, V. Nicolosi, L. Colombo, A. Fert, M. Garcia-Hernandez, A. Bachtold, G. F. Schneider, F. Guinea, C. Dekker, M. Barbone, C. Galiotis, A. Grigorenko, G. Konstantatos, A. Kis, M. Katsnelson, C. W. J. Beenakker, L. Vandersypen, A. Loiseau, V. Morandi, D. Neumaier, E. Treossi, V. Pellegrini, M. Polini, A. Tredicucci, G. M. Williams, B. H. Hong, J. H. Ahn, J. M. Kim, H. Zirath, B. J. Van Wees, H. Van Der Zant, L. Occhipinti, A. Di Matteo, I. A. Kinloch, T. Seyller, E. Quesnel, X. Feng, K. Teo, N. Rupesinghe, P. Hakonen, S. R. T. Neil, Q. Tannock, T. Löfwander, J. Kinaret, *Nanoscale* **2015**, *7*, 4598.
[40] F. Bonaccorso, L. Colombo, G. Yu, M. Stoller, V. Tozzini, A. C. Ferrari, R. S. Ruoff, V. Pellegrini, *Science* **2015**, *347*, 1246501.
[41] Z. Y. Yin, J. X. Zhu, Q. Y. He, X. H. Cao, C. L. Tan, H. Y. Chen, Q. Y. Yan, H. Zhang, *Adv. Energy Mater.* **2014**, *4*, 1300574.
[42] G. Calogero, A. Bartolotta, G. Di Marco, A. Di Carlo, F. Bonaccorso, *Chem. Soc. Rev.* **2015**, DOI: 10.1039/C4CS00309H.
[43] C. T. G. Smith, R. W. Rhodes, M. J. Beliatis, K. D. G. I. Jayawardena, L. J. Rozanski, C. A. Mills, S. R. P. Silva, *Appl. Phys. Lett.* **2014**, *105*, 073304.
[44] M. J. Beliatis, K. K. Gandhi, L. J. Rozanski, R. Rhodes, L. McCafferty, M. R. Alenezi, A. S. Alshammari, C. A. Mills, K. D. G. Jayawardena, S. J. Henley, S. R. P. Silva, *Adv. Mater.* **2014**, *26*, 2078.
[45] V. Georgakilas, M. Otyepka, A. B. Bourlinos, V. Chandra, N. Kim, K. C. Kemp, P. Hobza, R. Zboril, K. S. Kim, *Chem. Rev.* **2012**, *112*, 6156.
[46] A. Kuc, T. Heine, G. Seifert, *Phys. Rev. B* **2010**, *81*, 085430.
[47] Y. H. Lu, W. Chen, Y. P. Feng, P. M. He, *J. Phys. Chem. B* **2009**, *113*, 2.
[48] J. E. Johns, M. C. Hersam, *Acc. Chem. Res.* **2013**, *46*, 77.
[49] C. Shim, M. Kim, S. G. Ihn, Y. S. Choi, Y. Kim, K. Cho, *Chem. Commun.* **2012**, *48*, 7206.
[50] O. M. Maragó, F. Bonaccorso, R. Saija, G. Privitera, P. G. Gucciardi, M. A. Iatì, G. Calogero, P. H. Jones, F. Borghese, P. Denti, V. Nicolosi, A. C. Ferrari, *ACS Nano* **2010**, *4*, 7515.
[51] M. Lotya, Y. Hernandez, P. J. King, R. J. Smith, V. Nicolosi, L. S. Karlsson, F. M. Blighe, S. De, Z. Wang, I. T. McGovern, G. S. Duesberg, J. N. Coleman, *J. Am. Chem. Soc.* **2009**, *131*, 3611.
[52] T. J. Mason, *Sonochemistry*, Oxford University, New York **1999**, Ch. 1.
[53] Y. Hernandez, V. Nicolosi, M. Lotya, F. M. Blighe, Z. Sun, S. De, I. T. McGovern, B. Holland, M. Byrne, Y. K. Gun'Ko, J. J. Boland,P. Niraj,G. Duesberg, S. Krishnamurthy, R. Goodhue, J. Hutchison, V. Scardaci, A. C. Ferrari, J. N. Coleman, *Nat. Nanotechnol.* **2008**, *3*, 563.
[54] F. Bonaccorso, A. Lombardo, T. Hasan, Z. Sun, L. Colombo, A. C. Ferrari, *Mater. Today* **2012**, *15*, 564.
[55] J. Hassoun, F. Bonaccorso, M. Agostini, M. Angelucci, M. G. Betti, R. Cingolani, M. Gemmi, C. Mariani, S. Panero, V. Pellegrini, B. Scrosati, *Nano Lett.* **2014**, *14*, 4901.
[56] D. L. Greenaway, G. Harbeke, F. Bassani, E. Tosatti, *Phys. Rev.* **1969**, *178*, 1340.
[57] V. G. Kravets, A. N. Grigorenko, R. R. Nair, P. Blake, S. Anissimova, K. S. Novoselov, A. K. Geim, *Phys. Rev. B* **2010**, *81*, 155413.
[58] L. Yang, J. Deslippe, C. H. Park, M. L. Cohen, S. G. Louie, *Phys. Rev. Lett.* **2009**, *103*, 186802.
[59] J. C. Meyer, A. K. Geim, M. I. Katsnelson, K. S. Novoselov, T. J. Booth, S. Roth, *Nature* **2007**, *446*, 60.
[60] A. C. Ferrari, J. Robertson, *Phys. Rev. B* **2000**, *61*, 14095.
[61] A. C. Ferrari, D. M. Basko, *Nat. Nanotechnol.* **2013**, *8*, 235.
[62] A. C. Ferrari, J. C. Meyer, V. Scardaci, C. Casiraghi, M. Lazzeri, F. Mauri, S. Piscanec, D. Jiang, K. S. Novoselov, S. Roth, A. K. Geim, *Phys. Rev. Lett.* **2006**, *97*, 187401.
[63] A. C. Ferrari, J. Robertson, *Phys. Rev. B* **2001**, *64*, 075414.
[64] C. Casiraghi, A. Hartschuh, H. Qian, S. Piscanec, C. Georgi, A. Fasoli, K. S. Novoselov, D. M. Basko, A. C. Ferrari, *Nano Lett.* **2009**, *9*, 1433.
[65] M. Naebe, J. Wang, A. Amini, H. Khayyam, N. Hameed, L.-H. Li, Y. Chen, B. Fox, *Sci. Rep.* **2014**, *4*, 4375.
[66] P. V. Kumar, N. M. Bardhan, S. Tongay, J. Wu, A. M. Belcher, J. C. Grossman, *Nat. Chem.* **2014**, *6*, 151.
[67] J. Zhu, J. Yang, B. Deng, *Environ. Chem. Lett.* **2010**, *8*, 277.
[68] Y. Xu, Z. Liu, X. Zhang, Y. Wang, J. Tian, Y. Huang, Y. Ma, X. Zhang, Y. A Chen, *Adv. Mater.* **2009**, *21*, 1275.
[69] S. Niyogi, E. Bekyarova, M. E. Itkis, J. L. McWilliams, M. A. Hamon, R. C. Haddon, *J. Am. Chem. Soc.* **2006**, *128*, 7720.
[70] S. Stankovich, R. D. Piner, S. T. Nguyen, R. S. Ruoff, *Carbon* **2006**, *44*, 3342.

[71] E. Bekyarova, M. E. Itkis, P. Ramesh, C. Berger, M. Sprinkle, W. A. de Heer, R. C. Haddon, *J. Am. Chem. Soc.* **2009**, *131*, 1336.
[72] F. Tuinstra, J. L. Koenig, *J. Chem. Phys.* **1970**, *53*, 1126.
[73] C. M. Cardona, W. Li, A. E. Kaifer, D. Stockdale, G. C. Bazan, *Adv. Mater.* **2011**, *23*, 2367.
[74] G. G. Malliaras, J. R. Salem, P. J. Brock, C. Scott, *Phys. Rev. B* **1998**, *58*, 13411.
[75] V. Shrotriya, Y. Yao, G. Li, Y. Yang, *Appl. Phys. Lett.* **2006**, *89*, 063505.
[76] Y. Zhao, D. G. Truhlar, *Theor. Chem. Acc.* **2008**, *120*, 215.
[77] J. Tomasi, B. Mennucci, R. Cammi, *Chem. Rev.* **2005**, *105*, 2999.
[78] S. Osella, A. Narita, M. G. Schwab, Y. Hernandez, X. Feng, K. Müllen, D. Beljonne, *ACS Nano* **2012**, *6*, 5539.
[79] J. Heyd, G. E. Scuseria, M. Ernzerhof, *J. Chem. Phys.* **2003**, *118*, 8207.
[80] M. J. Frisch, G. W. Trucks, H. B. Schlegel, G. E. Scuseria, M. A. Robb, J. R. Cheeseman, G. Scalmani, V. Barone, B. Mennucci, G. A. Petersson, H. Nakatsuji, M. Caricato, X. Li, H. P. Hratchian, A. F. Izmaylov, J. Bloino, G. Zheng, J. L. Sonnenberg, M. Hada, M. Ehara, K. Toyota, R. Fukuda, J. Hasegawa, M. Ishida, T. Nakajima, Y. Honda, O. Kitao, H. Nakai, T. Vreven, J. A. Montgomery Jr, J. E. Peralta, F. Ogliaro, M. Bearpark, J. J. Heyd, E. Brothers, K. N. Kudin, V. N. Staroverov, R. Kobayashi, J. Normand, K. Raghavachari, A. Rendell, J. C. Burant, S. S. Iyengar, J. Tomasi, M. Cossi, N. Rega, J. M. Millam, M. Klene, J. E. Knox, J. B. Cross, V. Bakken, C. Adamo, J. Jaramillo, R. Gomperts, R. E. Stratmann, O. Yazyev, A. J. Austin, R. Cammi, C. Pomelli, J. W. Ochterski, R. L. Martin, K. Morokuma, V. G. Zakrzewski, G. A. Voth, P. Salvador, J. J. Dannenberg, S. Dapprich, A. D. Daniels, Ö. Farkas, J. B. Foresman, J. V. Ortiz, J. Cioslowski, D. J. Fox, *Gaussian 09*, Revision A.1, Gaussian, Inc., Wallingford, CT **2009**.
[81] F. Torrisi, T. Hasan, W. Wu, Z. Sun, A. Lombardo, T. S. Kulmala, G.-W. Hsieh, S. Jung, F. Bonaccorso, P. J. Paul, D. Chu, A. C. Ferrari, *ACS Nano* **2012**, *6*, 2992.
[82] M. M. Stylianakis, G. D. Spyropoulos, E. Stratakis, E. Kymakis, *Carbon* **2012**, *50*, 5554.
[83] G. Kakavelakis, E. Stratakis, E. Kymakis, *Chem. Commun.* **2014**, *50*, 5285.